Article

Not peer-reviewed version

InSAR Phase Linking with L2-CSLCs: Enhancing Infrastructure Monitoring Accuracy at Algeciras Port

Jaime Sánchez-Fernández , Alfredo Fernández-Landa * , Alvaro Hernández Cabezudo , Rafael Molina Sánchez

Posted Date: 2 October 2024

doi: 10.20944/preprints202410.0120.v1

Keywords: Phase linking; Coregistered SLCs; Algeciras Port; Geometric accuracy; ETAD corrections; Sentinel-1; Radar imaging

Article

InSAR Phase Linking with L2-CSLCs: Enhancing Infrastructure Monitoring Accuracy at Algeciras Port

Jaime Sánchez-Fernández [1,2,3], Alfredo Fernández-Landa [2,3,*], Álvaro Hernández Cabezudo [2,3] and Rafael Molina Sánchez [4]

[1] Escuela Técnica Superior de Ingenieros Navales, Universidad Politécnica de Madrid (UPM). Av. Universidad Politécnica de Madrid, 28040 Madrid, Spain
[2] Department of Land Morphology & Engineering, ETSI Caminos, Canales y Puertos, Universidad Politécnica de Madrid, 28040 Madrid, Spain
[3] Detektia Earth Surface Monitoring S.L., C/ Faraday 7, 28049 Madrid, Spain
[4] CEHINAV, DITTU, ETSI de Caminos, Canales y Puertos. Universidad Politécnica de Madrid. 28040 Madrid, Spain
* Correspondence: afernandez@detektia.com; Tel.: +34-644-081-332 (A.F.-L.)

Abstract: This paper presents an advanced methodology for processing radar imagery stacks using Persistent Scatterer and Distributed Scatterer Interferometry (PSDS) to enhance spatial coherence and improve displacement detection accuracy. The workflow leverages Level 2 Coregistered Single Look Complex (L2-CSLC) images generated by the open-source COMPASS (COregistered Multi-temPorAl Sar SLC) framework in combination with the Combined eigenvalue maximum likelihood Phase Linking (CPL) approach as implemented in MiaplPy. Starting the analysis directly from Level 2 products offers a significant advantage to end-users, as they simplify processing by being pre-geocoded and ready for immediate analysis. Additionally, the open-source nature of the workflow and the use of L2-CSLC products simplify the processing pipeline, making it easier to distribute directly to users for practical applications in monitoring infrastructure stability in dynamic environments. The ISCE3-MiaplPy workflow is compared against ISCE2-MiaplPy and the European Ground Motion Service (EGMS) to assess its performance in detecting infrastructure deformation in dynamic environments, such as the Algeciras port. Results indicate that ISCE3-MiaplPy delivers significantly denser measurements, albeit with increased noise, compared to its counterparts. This higher resolution enables a more detailed understanding of infrastructure stability and surface dynamics, which is critical for environments with ongoing human activity or natural forces.

Keywords: Phase linking; Coregistered SLCs; Algeciras Port; Geometric accuracy; ETAD corrections; Sentinel-1; Radar imaging

1. Introduction

The sustainability and resilience of port infrastructures are crucial for the global economy, as they directly impact trade, economic growth, and environmental conservation [1]. Implementing a timely and efficient maintenance strategy is crucial to monitor the regular operation of port infrastructures, especially as harsh environmental conditions in ports can deteriorate their structural functionality [2].

The monitoring and control of damage to port infrastructures lies in the need to develop advanced management strategies that require a deep understanding of the spatial and temporal evolution of damage during the useful life of the structures. In particular, high spatial and temporal resolution monitoring of the geometrical evolution of port infrastructure is a fundamental input in damage assessment. The geometrical evolution of a breakwater, its overtopping protection walls, or the sliding or tilting of a caisson is not a failure of a structure per se. The combination of three-dimensional behavior with climatic, geotechnical, or operational boundary conditions, or the existence of extraordinary actions on elements or sections of work, allows the prevention and prediction of mitigating and corrective actions aimed at maximizing safety and minimizing construction and operating costs. In this context, the definition of the concept of damage in port infrastructures, its evolution, and the methodologies used to evaluate its progression are of significant importance [3,4].

By monitoring and controlling damage, it becomes possible to assess structural stability and make informed decisions about maintenance, repair, and potential upgrades, thus contributing to

 doi:10.20944/preprints202410.0120.v1

the sustainability and resilience of the port infrastructure. Currently, port infrastructure monitoring relies on conventional topographic and geotechnical approaches. Common techniques for tracking subsidence and minor changes in engineering structures include precision surveying (leveling), inclinometers, UAV photogrammetry, laser scanning, and global navigation satellite systems [5]. Although contact methods utilizing accelerometers and fiber optics can rapidly monitor crucial construction points, they prove impractical for overseeing the entire infrastructure due to their time-consuming and budget-intensive nature.

These control and monitoring systems typically incur significant costs, which requires field instrumentation. Moreover, measurements are often either non-existent or not conducted at the required frequency. Topographic and geotechnical campaigns, when available, lack uniformity in terms of techniques, data resolution, and temporal continuity, thus complicating their analysis. The inherent complexity, lack of standardization, and frequent absence of digitization and data integration make it difficult to anticipate the long-term behavior of various components within port infrastructure, hindering the development of an effective early warning system.

Despite the existence of measurements to assess deformation and structural conditions, there is a notable scarcity of developed early warning systems. This scarcity poses a challenge in facilitating timely decision-making on when and to what extent interventions are necessary to prevent irreversible damage to port infrastructure. Satellite-based Interferometric Synthetic Aperture Radar (InSAR) technology could solve many of the problems and limitations of more traditional techniques, as i) it does not require instrumentation or on-site personnel, ii) it provides homogeneous and comparable historical ground motion information throughout the port, iii) it generates a high density of deformation monitoring points, iv) it can cover large areas in a cost-effective way [6], v) it allows constant updates and fine-tuning of warning systems.

InSAR has emerged as a critical tool for monitoring and analyzing dynamic landscapes, particularly in areas of intense human activity such as ports [7,8], in particular methodologies that exploit persistent and distributed scatterers (PSDS) such as MiaPLpy software (MIAmi Phase Linking software in PYthon) [9] using a coregistered stack processed with InSAR Scientific Computing Environment 2 (ISCE2) [10] have been successfully applied to the monitoring of ports [11], subsidence [12] and reservoirs [13],...

As a significant maritime hub, Algeciras Port is a gateway to international trade and logistics. Accurate and reliable spatial data are necessary to enable effective management and informed decision-making, making it a compelling real-world scenario for comparing various workflows.

However, traditional InSAR imaging techniques often encounter challenges related to geometric accuracy, particularly in regions characterized by complex topography and rapid environmental changes. This limitation directly affects the interpretation and exploitation of the results. In fact, with an uncertainty of a few meters in crowded areas, it is often difficult to accurately identify which object or structural element corresponds to a given InSAR scatterer [14]. To address these limitations, this study proposes a comprehensive methodology to obtain displacement time series using Sentinel-1 coregistered single look complex (S1-CSLC) data [15–17], this is a new type of product generated using InSAR Scientific Computing Environment 3 (ISCE3) [18] developed by the Observational Products for End Users of Remote Sensing Analysis (OPERA) team with corrections inspired by the Extended Timing Annotation Dataset (ETAD) [19]. The wrapped flattened phase produced is already coregistered to a common terrestrial grid, with corrections for the ionosphere and the troposphere phase delays, and can be used for interferometric applications. To preserve resolution and reduce noise in areas of low coherence, we estimate the interferograms by means of the Phase Linking (PL) algorithm [20] using the sequential Eigenvalue Based Maximum Likelihood Estimator (Sequential EMI) method [21] with the use of MiaPLpy (MIAmi Phase Linking software in PYthon) [9], resulting in a redundant Delaunay network of interferograms and select the best of them based on the connected components created during the unwrapping. Finally, we invert for the displacement time series.

 doi:10.20944/preprints202410.0120.v1

To validate our approach, we compared the results of the ISCE3-MiaplPy workflow with the original approach presented by Mirzaee et al. [9] here referred to as ISCE2-MiaplPy and by using the same dates as the 2018-2022 of the European Ground Motion Service (EGMS) we could easily compare the time series near the measurement points between the three processes.

In summary, the present work aims to provide a workflow for generating InSAR deformation point clouds in port environments: 1) improving scatterer geolocation and point density by applying novel InSAR PSDS phase linking method and SLC co-registered with ETAD corrections, 2) facilitating the interpretation and analysis of results by generating georeferenced InSAR intermediate products, and 3) optimizing the quality of the results by filtering the best interferograms using connected components as criteria. The proposed workflow aims to contribute to the assignment of InSAR deformation time series to specific structural elements of port infrastructure.

2. Area of Study

The study area is located in the port of Algeciras in the Bay of Algeciras in southern Spain. This port is a crucial maritime hub in Europe and a significant gateway to the Mediterranean Sea.

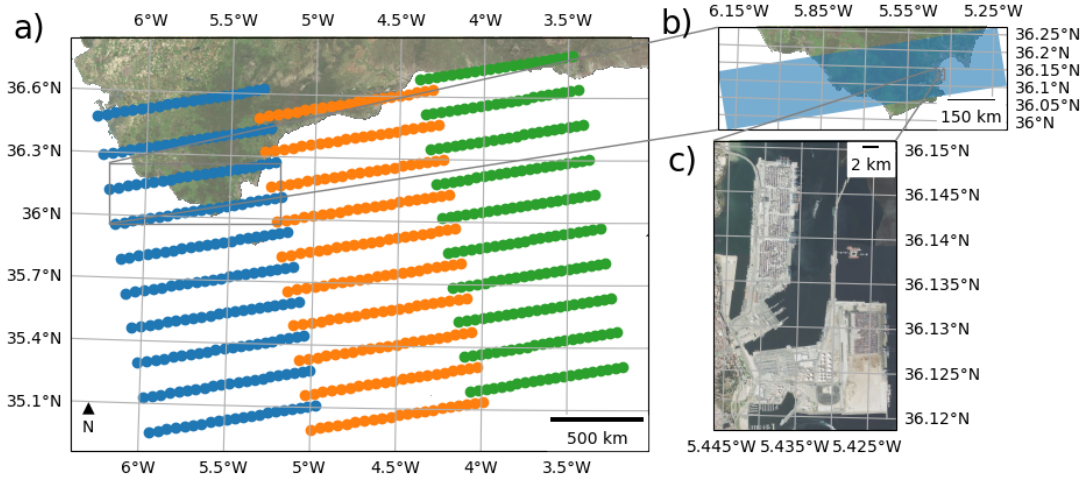

Figure 1. (**a**) Three swaths from the Interferometric Wide Swath mode ascending Track 74. Algeciras port is located in the IW1. (**b**) Burst t074-157011-iw1 processed (**c**) AOI processed with PSDS software.

The port of Algeciras Bay is a key player in the western Mediterranean, with a scale-free maritime network [22]. It serves as a gateway city connecting Europe and Africa and has experienced significant transformations in recent years [23]. The port's competitiveness in container traffic is influenced by factors such as transshipment and maritime accessibility [24]. In terms of efficiency, it ranks among the top Spanish ports, particularly in transshipment activities [25].

3. Data Used

3.1. EGMS

The results obtained in this work have been compared with the European Ground Motion Service (EGMS) level 2a product [26] using the 2018-2022 update [27]. EGMS provides homogeneous information on ground movements in Europe on a continental scale and updates annually. EGMS processes the same source of SAR information as used in this work from Sentinel-1A and Sentinel-1B twin satellites of the Copernicus Program from the European Union.

EGMS products are made by a consortium comprising four different InSAR Processing Entities (IPE). Consequently, there are differences in the processing algorithms implemented in the different processing chains, although all are based on advanced PS and DS InSAR processing techniques, the end products have the same attributes and all meet the project requirements in terms of quality, consistency,

 doi:10.20944/preprints202410.0120.v1

and homogeneity. Overlaps between adjacent processing areas are also used to check and ensure seamless harmonization between adjacent Sentinel-1 tracks and the different processing chains.

3.2. Sentinel 1 A and B dataset

A total of 270 SAR images were processed, including both ascending and descending geometries from Sentinel-1 constellation satellites A and B. All images are single-look complex (SLC) TOPSAR data acquired in Interferometric Wide (IW) swath mode with VV polarization for the time frame of 10 Jan 2020 to 27 Dec 2022. Coinciding with the temporal extent of the EGMS 2023 update.

Table 1. Sentinel 1 images used

Satellite	Ndates	First date	Last date	Geometry	Track
Sentinel-1A	150	2018/01/10	2022/12/27	Ascending	74
Sentinel-1B	120	2018/01/04	2021/12/14	Ascending	74

Precise orbit files produced within 20 days of the sensing time with an accuracy margin of 5 cm in 3D RMS are employed for image processing.

3.3. Copernicus DEM

The Copernicus Digital Elevation Model (DEM) Cop-GLO30 [28] has been used throughout the InSAR processing chain in this work. This is the same DEM used by EGMS. The Copernicus DEM is derived from the WorldDEM, an edited Digital Surface Model that features flattened water bodies, consistent river flows, and edited shorelines, coastlines, airports, and terrain structures. The WorldDEM product is based on radar satellite data from the TanDEM-X mission.

3.4. ETAD Dataset

State-of-the-art corrections for the most important sources of error in TOPS interferometry. Precise geolocalization (CSLC experiments accuracy) Sentinel-1 Extended Timing Annotation Processor (SETAP) [19,29].

3.5. Tropospheric and Ionospheric Information

For the estimation and subtraction of the tropospheric delay we used RAiDER [30], the weather model date used for the troposphere layer was ERA5 [31], while the IONEX NASA product [32] was used for the ionosphere Total Electron Content (TEC).

4. Methods

The proposed method (Figure 2) involves first generating a stack of Coregistered Single-Look Complex (CSLC) data. Subsequently, both Persistent Scatterer (PS) and Distributed Scatterer (DS) information are exploited over a stack segment using phase linking to obtain displacement time series.

 doi:10.20944/preprints202410.0120.v1

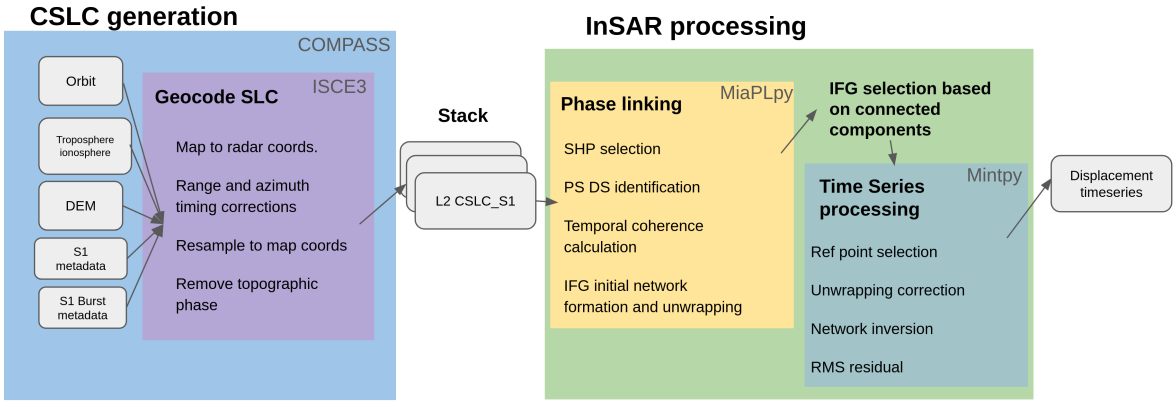

Figure 2. CSLCs processing schema.

Level 0 (L0) products consist of compressed and unfocused raw data. The Level 1 (L1) products are focused georeferenced data using orbit and attitude information from the satellite, provided in slant-range geometry. In contrast, Level 2 (L2), as the co-registered single look complex (L2-CSLC) [15] products derived from the L1 single look complex (SLC) product, are outputted in the projected map system, making it ready for analysis.

In the phase linking step, the coherence matrix of each image pixel is estimated, representing all possible interferograms over a set of N images for that pixel. The absolute values of the coherence matrix represent the interferometric correlation, ranging between 0 and 1, while the phase of the off-diagonal elements corresponds to the averaged phase of each interferogram. The coherence matrix of an ideal PS shows all correlation values equal to 1. An optimum set of N phase values is then extracted from each matrix. Following the Maximum Likelihood Estimation (MLE) of the optimum phase values, the process continues as with standard PSI algorithms. SqueeSAR® [33] is one example of such algorithms.

For validation purposes, we will be comparing the ISCE3-MiaPlPy workflow with EGMS as well as the same ISCE2-MiaPlPy which starts from normal L1-SLC to generate the coregistered stack using the ISCE2 TopStack processor [10].

4.1. Coregistered CSLC Stack

Regular Sentinel-1 SLC products are provided in a range-Doppler coordinate system and the grid is not aligned over multiple aqcuisitions so a coregistration process is normally used to align all images to the reference system of the master. CSLC coregistration output is provided in the chosen Coordinate Reference System (CRS), all images are resampled to a common grid of 10mx5m in Northing and Easting coordinates [34], and S1 Instrument Processing Facility (IPF) artifacts (i.e., bistatic delay, geometry steering Doppler and azimuth FM-rate mismatch) [29], atmospheric effects (i.e., ionosphere and static troposphere) and the Solid Earth tides effect [35] are estimated and removed.

The geocoded SLC phase is adjusted using a reference orbit and a DEM to eliminate the topographic phase components [36]. The CSLC product's sampling interval along the map's coordinate directions is comparable to that of the original full-resolution SLC product. Nonetheless, before resampling and interpolation of the data, the linear slope introduced by the electronic steering of the antenna needs to be corrected [37].

Since the CSLC phase is flattened, the phase difference between two CSLC products acquired on the same relative orbit produces an interferogram referring only to surface displacement and noise (i.e., no topographic fringes). This product specification includes definitions for auxiliary static datasets that contain rasterized data on Line of Sight (LOS), incidence angle, coordinates, layover, and shadow masks for each point, along with processing quality assurance information. The CSLC product can

 doi:10.20944/preprints202410.0120.v1

be opened with any GIS software or integrated with other geographic data products to generate interferograms and other applications.

4.1.1. Timing Corrections

ETAD gridded corrections for S-1 are applied to the SLC data for each burst, with the positions of the original pixels defined by the annotated time coordinates (t, τ). Initially, the time-annotated ETAD correction grids must be resampled to the SLC resolution using a simple bilinear interpolation. The combined ETAD range corrections, $\Delta_\tau(t, \tau)$, and azimuth corrections, $\Delta_t(t, \tau)$, are then subtracted from the original SLC slant range and azimuth timings, resulting in an irregularly gridded but timing-corrected SLC dataset. The different timing corrections applied.

- Range shift due to doppler: Due to the fact that a single transmitted radar pulse is reflected by different targets with different sensor-to-target geometries, several Doppler shifts are superimposed within one received range line. Therefore, a compensation of the Doppler effect immediately after receiving is not possible, this is translated as a range shift in TOPS interferometry [38]:

$$\Delta\tau_{Doppler} = -\Delta f_{Doppler}(t)/K_r \tag{1}$$

  Where $\Delta f_{Doppler}$ is the total doppler (geometric doppler + steering doppler) and K_r is the FM-rate of the range chirp [38–41]
- Bistatic Azimuth Effects Mitigation: The IPF applies the stop-and-go approximation in the processing of the S-1 acquisitions that assumes that the satellite is in the same position for the emission and reception, in reality the motion of the platform between pulses amounts to tens of meters that produces a shift in azimuth. To correct this effect we must reverse the original shift and apply the precise one:

$$\Delta t_{BA} = \tau_{mid}/2 - \tau_g/2 - rank \cdot PRI \tag{2}$$

  Here, τ_{mid} denotes the reconstructed mid-swath range time, τ_g stands for the range time at the correction grid point, and PRI corresponds to the pulse repetition interval for the burst in question. The parameter *rank* indicates the number of PRI events between the transmission of the pulse and the reception of its echo.
- Azimuth FM mismatch mitigation: This is a topography-correlated error that stems from a constant effective velocity parameter used in azimuth FM rate calculation during the processing of extensive azimuth blocks. For stripmap SAR with zero-Doppler steering, the mismatch effect (quadratic phase error) primarily causes image defocusing. However, for TOPS products, it also results in azimuth shifts.

- Solid Earth tides refer to the distortions in the Earth's crust due to the gravitational influences of the Sun and the Moon. These deformations usually fluctuate by +-25 cm vertically, and there is also notable horizontal movement reaching up to 6 cm. For the calculation we use Python-based solid Earth tides (PySolid) [35,42].

- Ionosphere delay in line-of-sight direction calculated from the TEC obtained from IONEX NASA product [32].

- Wet and dry LOS tropospheric delay: containing the LOS wet and dry troposphere delays computed from the respective dry and wet pressure obtained from the ERA5 model [31] preprocessed with RAiDER [30].

 doi:10.20944/preprints202410.0120.v1

4.2. Phase Linking

[9,21,43] [20,44,45] Following coregistration, the geocoded stack of radar images is subjected to phase linking, a critical step in consolidating spatial information across multiple acquisitions. Phase linking involves the coherent combination of radar images to generate a composite image with enhanced clarity and resolution. Using the precise geometric alignment achieved through coregistration, phase linking minimizes phase inconsistencies and artifacts, yielding a seamless and coherent representation of the observed area. The resultant composite image serves as a valuable resource for various applications, including but not limited to vessel tracking, land cover classification, and change detection within the Algeciras port.

4.2.1. PSDS Preprocessing

The first approach developed to estimate the deterministic component of the observer phases in coregistered InSAR stacks was persistent scatterer interferometry (PSI), which relies on bright scatterers smaller than the resolution cell with a good signal-to-noise ratio (SNR) . Another family of algorithms uses Distributed Scatterers, which are usually multiple smaller scatterers that share statistical characteristics over an extended area and experience decorrelation during the time series. The first algorithm to use this was the Small BAseline Subset (SBAS) technique [46], which uses reduced spatial resolution and limits itself to the most coherent interferograms to overcome decorrelation effects. The other approach used is PL which employs all the possible interferograms with the observation dates; this enhances the SNR and consequently also improves the displacement detection accuracy.

For a pixel at location x in a CSLC stack, a complex N × 1 target vector d is given by:

$$d_x(A,\theta) = \left[A_1 e^{i\theta_x^1}, A_2 e^{i\theta_x^2}, ..., A_N e^{i\theta_x^N},\right] \tag{3}$$

To take full advantage of the interferometric information, we estimate the N x N covariance matrix for a pixel P. We first need to find a neighborhood with Statistical Homogeneous Pixels (SHP)[33]; in order to find these groups of pixels, we evaluate the homogeneous similarity of the surroundings using a Kolmogorov-Smirnov test in a 15x15 square patch around each pixel. Once we have the SHPs, the complex covariance matrix (CCM) is defined as follows[**?**]:

$$\hat{C}_{ij} = \frac{1}{N_{SHP_p}} \sum_{x \in SHP_p} d_x^i {d_x^j}^* \tag{4}$$

Where * denotes the complex conjugation operation and N_{SHP} is the total number of SHP groups. The coherence matrix is defined as the magnitude of the CCM normalized by the amplitude:

$$|\hat{\Gamma}_{ij}| = |\hat{C}_{ij}| / \sqrt{\sum_{x \in SHP_p} d_x^i {d_x^i}^* \sum_{x \in SHP_p} d_x^j {d_x^j}^*} \tag{5}$$

This matrix is the maximum likelihood estimation of the second order moment for the SAR data over a neighbourhood of pixels. Different PL methods asume different factorization model for the coherence matrix [47], under this assumption computing the estimated wrapped phases corresponds to computing the eigenvector corresponding to the minimum eigenvalue of the following product:

$$(|\hat{\Gamma}|^{-1} \circ \hat{\mathbf{\Gamma}})\hat{\boldsymbol{v}} = \lambda_m \hat{\boldsymbol{v}} \tag{6}$$

Where $\circ$ denotes the Hadamard product. This method requires the $|\hat{\Gamma}|^{-1}$ to be semidefinite positive, if this is not true even after adding reguralization to the inversion, we just take the largest eigenvector of the CCM. This method is referred to as Combined eigenvalue maximum likelihood Phase Linking (CPL)[9].

 doi:10.20944/preprints202410.0120.v1

Under this model, the scattering characteristics of the DS region are estimated by a mechanism similar to PS. The MLE can be viewed as a temporal filter that reduces the data from n(n - 1)/2 interferograms to a phase sequence of length n.

The biggest disadvantage of this method is the increase in computational complexity involved in the computation of the full coherence matrix for each pixel, to avoid this we use a sequential estimator [48], which only needs partial access to the stack and uses virtual images created from mini-stacks of a determined size l. These ministacks are isolated diagonal blocks from the coherence matrix $\hat{\mathbf{\Gamma}}$ that are compressed temporally and then used to create artificial interferograms with newer ministacks and the latest acquisitions $l - 1$ in order to efficiently retrieve the long-term filtered coherent phase [44].

For a pixel to be selected as a PS it should have less than 10 SHP, its amplitude dispersion index [49] should be less than 0.4 and the top eigenvalue contribution in the decomposition of Γ is 70%. The CSLC phase for these pixels in the stack is referenced to the initial acquisition and saved as their wrapped phase series, with their temporal coherence assigned a value of 1. [9], this criteria allows us to improve the PS density and filter pixels where multi-target layover is present [50].

Once the phase linking step is completed, we need to create a network of interferograms for unwrapping. In our method, we create a Delaunay network with an increased temporal threshold, in order to have redundant interferograms and then unwrap them using SNAPHU [51]. Once all interferograms have been unwrapped, we use the connected components layer created for each interferogram to find the most connected points and discard the interferograms in which they are disconnected above a defined threshold. This allows us to optimize Miami INsar Timeseries software in PYthon (MInTPy) unwrapping error correction capabilities.

Finally, we invert the displacement time series using regularized least squares with an L1 norm, weighted by the temporal coherence of the phase linking step.

5. Results

5.1. Impact of Timing Corrections on Geocoded SLC Data

Figure 3 presents the timing corrections applied during the coregistration of a raw Sentinel-1 burst. These corrections address delays caused by atmospheric effects, tidal deformations from celestial bodies, and internal adjustments within the Sentinel-1 SAR-IPF system [15]. These corrected timings are crucial for ensuring accurate geolocation and subpixel-level feature analysis in repeat-pass interferometry [19]. These corrections are generated using a coarse grid and then upscaled to match the original SLC.

 doi:10.20944/preprints202410.0120.v1

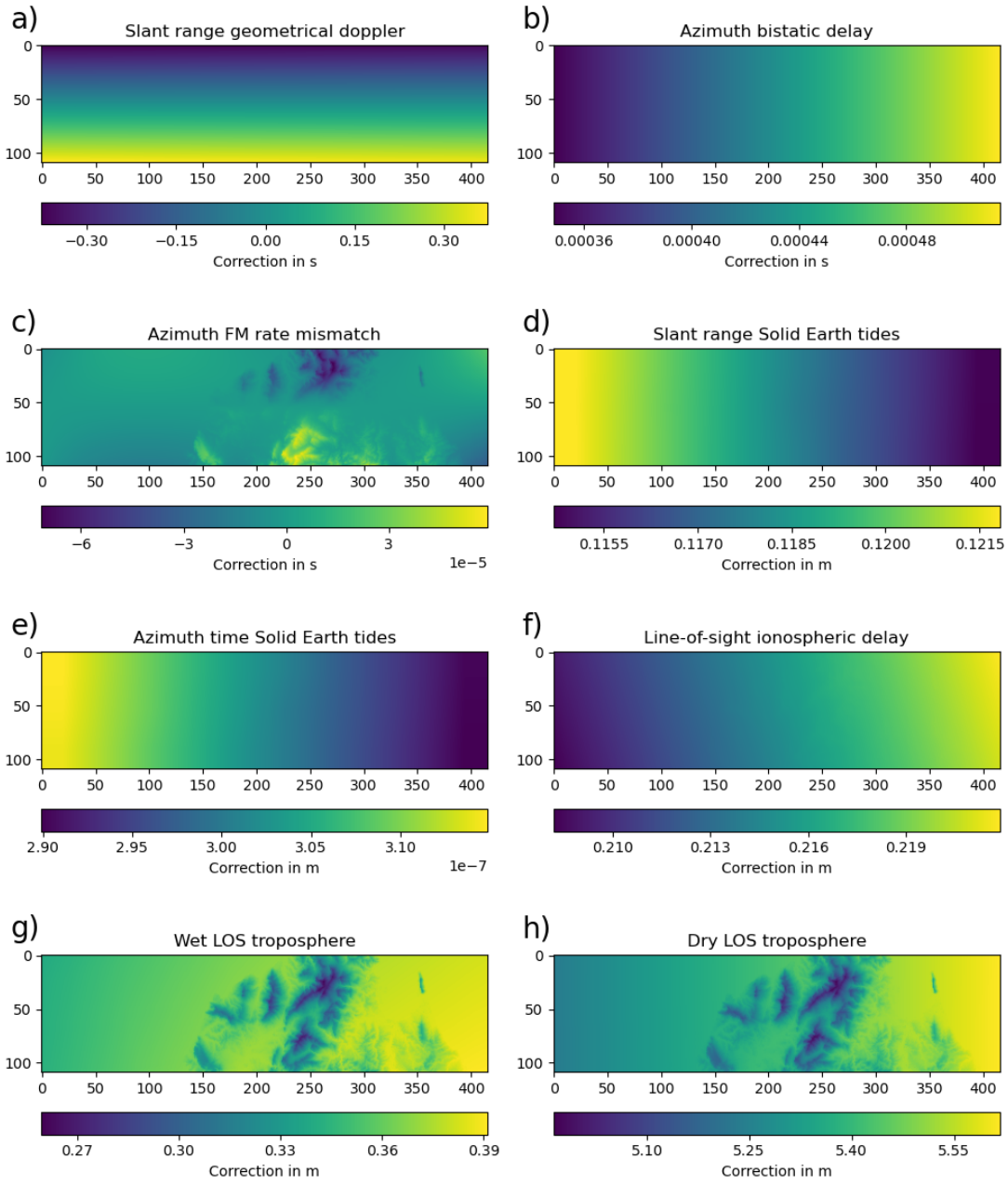

Figure 3. Coregistered SLC timing corrections for 24/03/2020. (**a**) Slant range geometrical doppler (**b**) Azimuth bistatic delay (**c**) Azimuth FM rate mismatch (**d**) Slant range Solid Earth tides (**e**) Azimuth time Solid Earth tides (**f**) Line-of-sight ionospheric delay (**g**) Wet LOS troposphere (**h**) Dry LOS troposphere.

Timing corrections effectively mitigate errors in range and azimuth dimensions, thereby enhancing the alignment of data across repeated observations. This improved alignment is essential for reliable subsequent analyses, as it directly impacts the accuracy of geocoded SLC products.

5.2. Construction and Optimization of the InSAR Network

We constructed an initial redundant network of 780 interferograms over a 3-year period using Delaunay triangulation, with a maximum temporal distance between interferograms of 220 days and a perpendicular baseline of 200 m (Figure 4). This high redundancy allowed for the selection of interferograms that maximize the number of connected components, increasing the number of fully connected pixels from 1,241 to 2,937.

Preprints.org (www.preprints.org) | NOT PEER-REVIEWED | Posted: 2 October 2024 doi:10.20944/preprints202410.0120.v1

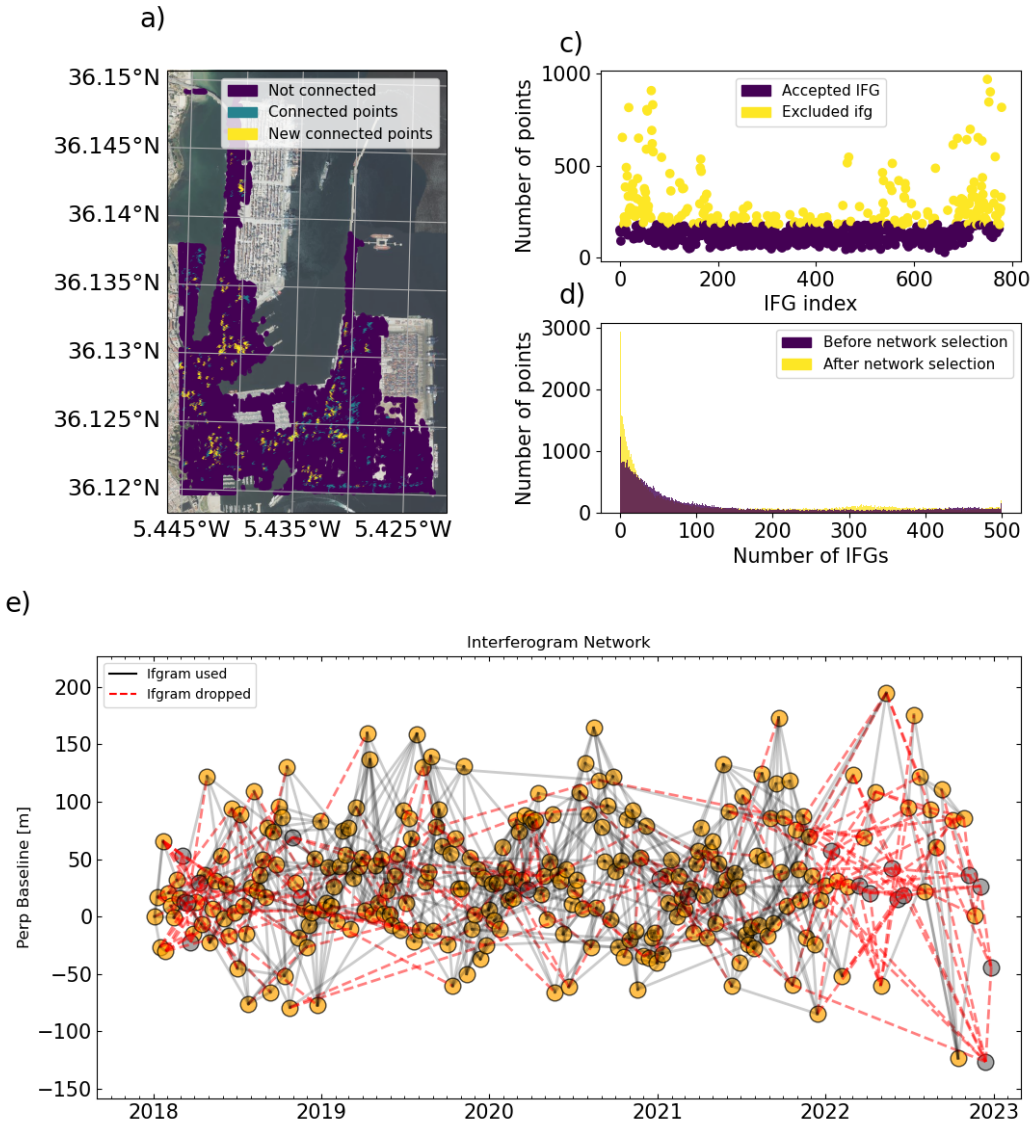

Figure 4. InSAR network selection. (**a**) Mask connected components before (purple) and after (yellow) IFG selection (**b**) Number of connected components (**c**) Number of not connected pixels per interferogram (**d**) Number of interferograms not connected per pixel (**e**) IFG network selected.

As shown in Figure 4, the areas with the lowest sum of connected components are located in regions of high port activity, such as the general cargo and container areas and the Juan Carlos I Pier in the Northeast of the AOI. The frequent movement of containers and docked vessels in these areas is likely to cause decorrelation, leading to fewer connected components.

This optimization of the interferogram network significantly improves the reliability of the InSAR analysis, particularly in dynamic environments, as it allows us to preserve the most points in the connected component mask needed for the phase closure correction in Mintpy processing [52].

5.3. Temporal Coherence and Amplitude Dispersion Analysis

Figure 5 illustrates the spatial distribution of temporal coherence and amplitude dispersion across the AOI. Temporal coherence is near 1 for persistent scatterers, indicating high stability over time, while lower coherence is observed for distributed scatterers (DS). The amplitude dispersion is significantly higher in man-made structures, probably because of strong reflections.

 doi:10.20944/preprints202410.0120.v1

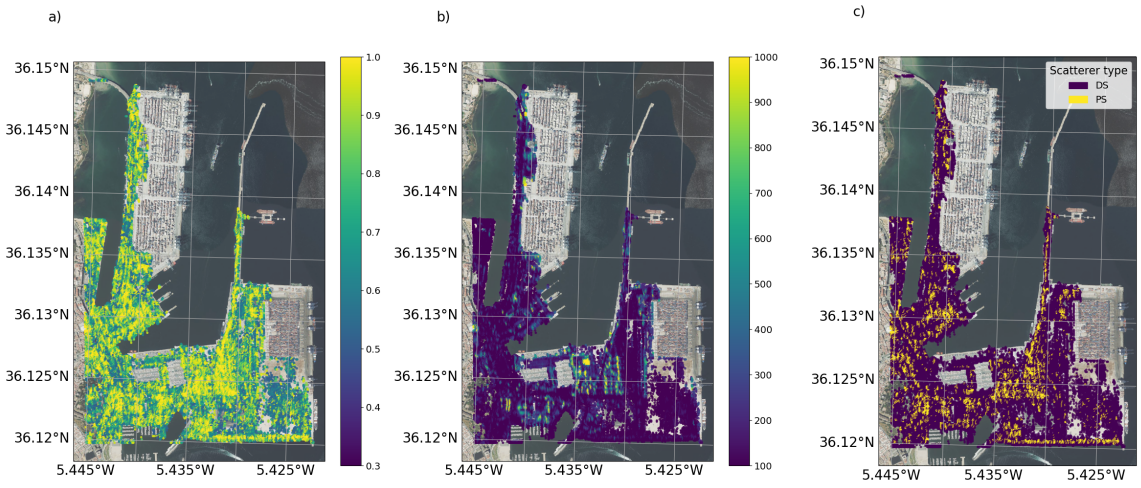

Figure 5. (**a**) Temporal coherence (**b**) Amplitude dispersion. (**c**) Scatterer type.

These patterns suggest that persistent scatterers dominate stable areas, as we can see in Figure 5, while DSs are more prevalent in regions with dynamic activity, such as port facilities. This distinction is crucial for interpreting the stability and movement within the AOI, particularly when analyzing long-term displacement patterns.

5.4. Comparison of Velocity Estimations Using Different Processing Workflows

The velocities for all points in the AOI were calculated using three different processing methodologies: EGMS, ISCE2-MiaplPy, and ISCE3-MiaplPy. As shown in Figure 6 and Table 2, ISCE3-MiaplPy produced the highest density of measurement points, with an increase of more than 300% compared to EGMS and an increase of 130% compared to ISCE2-MiaplPy. This increase is likely due to the higher resampled resolution of CSLC in ISCE3, as well as the application of the eigenvalue criterion [50] in both ISCE2 and ISCE3, which increases the density of PS and includes DS that are sparse in EGMS.

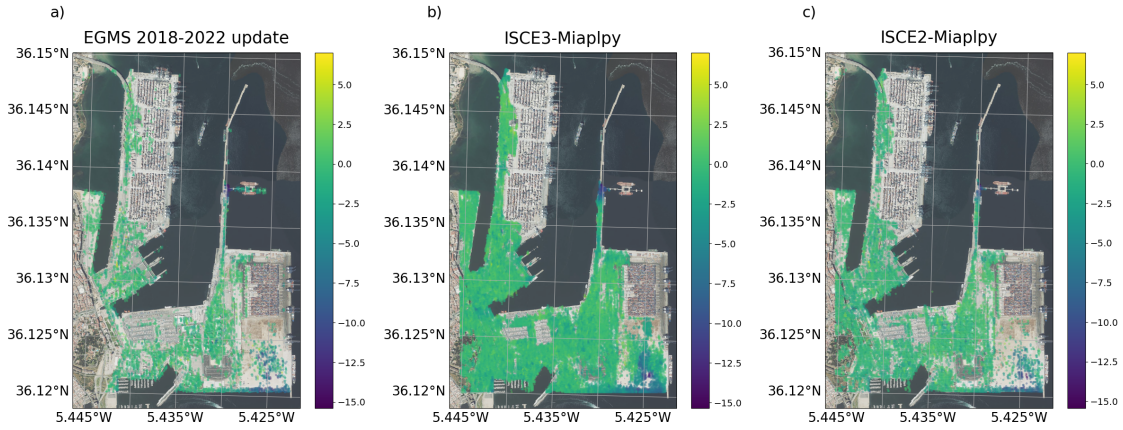

Figure 6. (**a**) EGMS velocity for the Algeciras port (**b**) Same area processed using CSLCs and phase (**c**) Same area processed using ISCE2 and geocoding after phase linking.

Table 2. Results summary for different workflows over the AOI

Workflows	Measurement points	Mean vel (mm/year)	STD (mm/year)
ISCE3-MiaPLPy	33142	-0.63	1.59
ISCE2-MiaPLPy	14061	-0.67	1.62
EGMS	8041	-0.95	2.12

 doi:10.20944/preprints202410.0120.v1

Comparison of velocity histograms (Figure 7) highlights the differences between these workflows. The ISCE3-MiaplPy process consistently provides more detailed and higher-resolution velocity estimates, particularly in areas with dense PS and DS distributions.

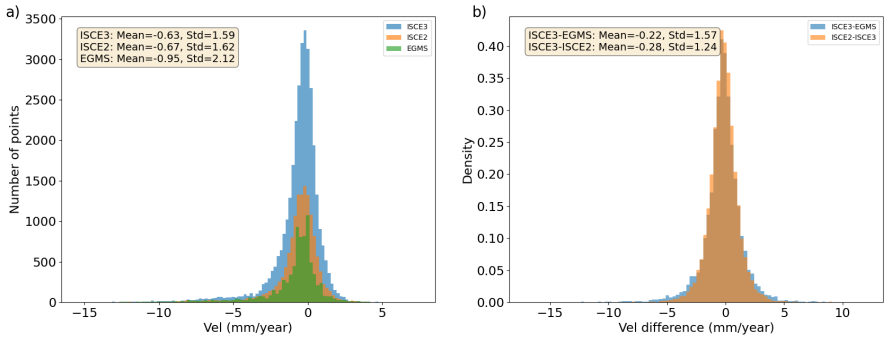

Figure 7. (**a**) Histograms for the velocity in ISCE3-MiaplPy, ISCE2-MiaplPy, and EGMS over the AOI (**b**) Histogram of velocity differences between ISCE3-EGMS and ISCE2-ISCE3.

In Figures 8 and 9, the time series analysis is focused on two critical areas within Algeciras Port: the EVOS terminal and the development area south of the Isla Verde Exterior breakwater. In the EVOS terminal (Figure 8), the deformation patterns observed using ISCE3 closely align with those detected by the EGMS dataset, with ISCE3 providing slightly better coverage. However, the ISCE3 time series data exhibit more noise, as the mean of the time series exhibits more variance in the ISCE3-MiaplPy process than in EGMS, which may obscure some subtle subsidence patterns. Similarly, in the development area near Isla Verde Exterior (Figure 9), all methods show consistent velocity trends, with ISCE3 offering greater spatial coverage but at the cost of increased noise.

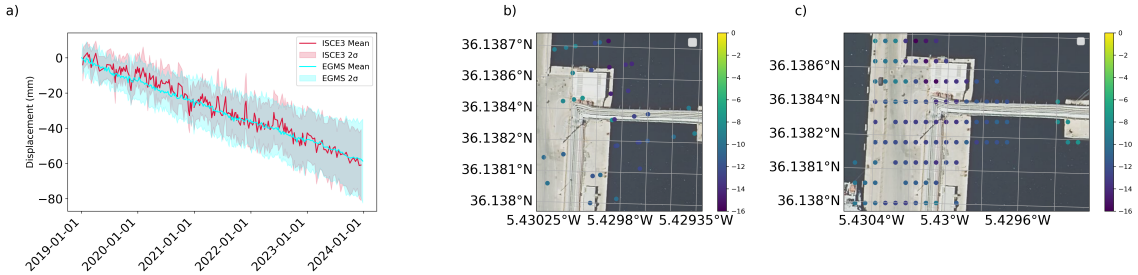

Figure 8. (**a**) Comparison of a group of timeseries over EVOS Terminal in ISCE3-MiaPLpy and EGMS (**b**) Measurement points over the area by EGMS colored by velocity. (**c**) Same for ISCE3-Miaplpy.

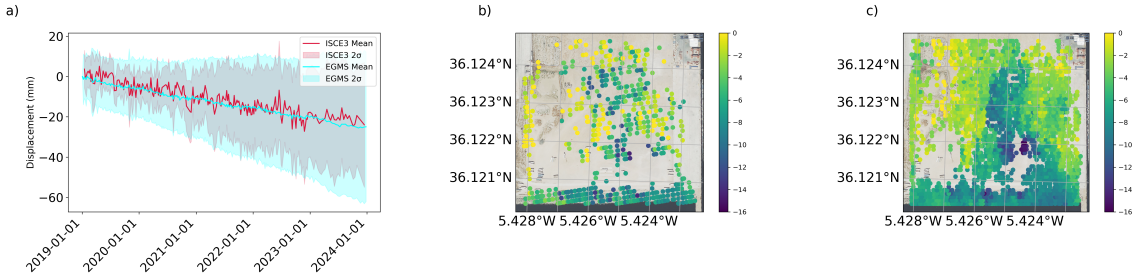

Figure 9. (**a**) Comparison of a group of timeseries over Isla Verde Exterior in ISCE3-MiaPLpy and EGMS (**b**) Measurement points over the area by EGMS colored by velocity. (**c**) Same for ISCE3-Miaplpy.

In general, the comparative analysis of these workflows indicates that, while ISCE3-MiaplPy offers improved coverage to detect deformation patterns across the AOI, it also introduces more noise

 doi:10.20944/preprints202410.0120.v1

into the time series. Despite these differences, general deformation trends are consistent across all methods, demonstrating their reliability monitoring areas with complex activity and infrastructure.

6. Discussion and Conclusions

In this article, we present a new methodology for PSDS processing [21] using L2-CSLC products, generated after L1-SLC images. To our knowledge, this is the first use case for MiaplPy software [9] using this type of L2 product. The resulting processing pipeline is completely open source. In order to validate our results, we compared it with ESA EGMS and also a different preprocessing methodology using ISCE2.

CSLC products simplify InSAR workflows as they allow users to start the interferometric processing directly without the need for preprocessing. Additionally, having fully coregistered intermediate products (such as temporal or spatial coherence, connected component masks, and amplitude dispersion) and the ability to quickly integrate them into any Geographic Information System significantly improves the interpretation of the results. As seen in Figure 5, many structures are apparent simply by analyzing amplitude dispersion, which enhances time series analysis. This improvement benefits both the InSAR expert and the end user, facilitating faster and more informed decision-making.

CSLC products simplify InSAR workflows as they can be distributed so that the user can start the interferometric processing directly without any preprocessing needed on their part. Additionally, having fully coregistered intermediate products (such as temporal or spatial coherence, connected component masks, amplitude dispersion, etc.) and the ability to quickly integrate them into any Geographic Information System substantially improves the interpretation of the results. As we can see in Figure 5, many structures are apparent just by looking at the amplitude dispersion, which can help time series analysis. This improvement in interpretation adds value to both the InSAR expert responsible for generating deformation results and the end user, facilitating decision making.

The results demonstrate that the ISCE3-MiaplPy workflow using L2-CSLC products leads to denser and more spatially coherent measurements compared to other workflows, providing a more detailed understanding of the stability of the infrastructure. Although the higher density of measurements introduces some trade-offs, such as increased noise, this level of detail proves especially valuable in dynamic environments like the port of Algeciras. The ability of the workflow to analyze key parameters, such as temporal coherence, amplitude dispersion, and phase closure, provides a nuanced assessment of how ongoing port operations, including the movement of ships and goods, impact infrastructure stability.

CSLC products include advanced timing error correction algorithms [19], yielding increasingly precise scatterer localization. This has been demonstrated in Point Target Analysis (PTA), achieving an absolute location error of 0.3 m in range and 0.5 m in azimuth for Sentinel-1 IW mode [29] and has also been replicated for CSLC products with similar results [53,54]. Our results align with these findings, further validating the utility of CSLC products for infrastructure monitoring.

An important factor to consider for future improvements is the quality of the DEM used for coregistration. Although we used the Copernicus DEM [28]to maintain consistency with EGMS [26,27], higher resolution DEMs from LiDAR or photogrammetric campaigns could further enhance geolocation accuracy, especially in port areas where abrupt elevation changes are common. Maintaining accurate location of scatterers is essential for correctly attributing measured deformations to specific structures, which is critical for detailed monitoring of failure modes in port infrastructure [55].

Looking ahead, several future research directions could build on this work. A key area of investigation is the effect of more accurate DEMs on improving coregistration, particularly in complex environments with substantial height variations. Additionally, exploring the use of different radar bands, such as combining the X-band with the C-band, may offer advantages in monitoring smaller or localized structures with higher resolution.

Further studies could also focus on expanding the application of this workflow to other types of port infrastructure, such as container terminals, storage silos, and piers. Developing a broader

 doi:10.20944/preprints202410.0120.v1

collection of failure modes linked to satellite data would be highly beneficial. This could ultimately lead to the creation of a warning system based on hypothesis testing, which allows real-time monitoring and risk mitigation of critical infrastructure in dynamic environments.

Author Contributions: Conceptualization, J.S.-F., A.F.-L. and R.M.S.; methodology, J.S.-F; software, J.S.-F and A.H.C.; validation, J.S.-F, A.F.-L., and R.M.S.; investigation, J.S.-F; writing—original draft preparation, J.S.-F; writing—review and editing, A.F.-L., A.H.C. and R.M.S.. All authors have read and agreed to the published version of the manuscript.

Funding: This research received public funds through the Industrial doctorates program DIN2020-011531, provided by the Ministry of Science and Innovation and the State Research Agency (MCIN/AEI/10.13039/501100011033) and by the European Union NextGenerationEU/PRTR initiative.

Data Availability Statement: The raw data supporting the conclusions of this article will be made available by the authors on request.

Acknowledgments: The authors would like to acknowledge the support of the Ports 4.0 Ports of Spain Tradetech Fund and the Autoridad Portuaria de Bahía de Algeciras. Special thanks to the OPERA Team at JPL and the Rosenstiel School of Marine and Atmospheric Science, University of Miami, for developing the open-source software suite that made the integrated workflow possible. The first author is supported by the Industrial Doctorates grant (DIN2020-011531).

Conflicts of Interest: The authors declare no conflicts of interest.

Abbreviations

The following abbreviations are used in this manuscript:

InSAR	Interferometric Synthetic Aperture Radar
PSDS	Persistent Scatterer and Distributed Scatterer
L2-CSLC	Level 2 Coregistered Single Look Complex
CPL	Combined eigenvalue maximum likelihood Phase Linking
COMPASS	COregistered Multi-temPorAl Sar SLC
EGMS	European Ground Motion Service
ISCE	InSAR Scientific Computing Environment
SLC	Single Look Complex
DEM	Digital Elevation Model
PNOA	National Aerial Orthophotography Plan
SBAS	Small BAseline Subset
SHP	Statistical Homogeneous Pixels
CCM	Complex Covariance Matrix
MLE	Maximum Likelihood Estimation
PTA	Point Target Analysis
ALE	Absolute Location Error
CRS	Coordinate Reference System
ETAD	Enhanced Timing Annotation Dataset
ERA5	ECMWF Reanalysis 5th Generation
MiaplPy	Miami InSAR Time-Series Software in Python
MintPy	Miami INsar Timeseries software in PYthon
Raider	Ray-tracing Atmospheric Delay Estimation for InSAR
OPERA	Open Platform for Earth Observation-Based Radar Applications
PSI	Persistent Scatterer Interferometry
PL	Phase Linking
IFG	Interferogram
LOS	Line of Sight

References

1. Pavlic, B.; Cepak, F.; Sucic, B.; Peckaj, M.; Kandus, B. Sustainable port infrastructure, practical implementation of the green port concept. *Thermal Science* **2014**, *18*, 935–948. doi:10.2298/TSCI1403935P.

2. Zhang, Y.; Kim, C.W.; Tee, K.F.; Lam, J.S.L. Optimal sustainable life cycle maintenance strategies for port infrastructures. *Journal of Cleaner Production* **2017**, *142*, 1693–1709. doi:10.1016/j.jclepro.2016.11.120.
3. Campos, A.; Molina-Sanchez, R.; Castillo, C. Damage in Rubble Mound Breakwaters. Part II: Review of the Definition, Parameterization, and Measurement of Damage. *Journal of Marine Science and Engineering* **2020**, *8*, 306. doi:10.3390/jmse8050306.
4. Castillo, C.; Castillo, E.; Fernández-Canteli, A.; Molina, R.; Gómez, R. Stochastic Model for Damage Accumulation in Rubble-Mound Breakwaters Based on Compatibility Conditions and the Central Limit Theorem. *Journal of Waterway, Port, Coastal, and Ocean Engineering* **2012**, *138*, 451–463. doi:10.1061/(ASCE)WW.1943-5460.0000146.
5. de Almeida, E.; van Gent, M.R.A.; Hofland, B. Damage Characterization of Rock Slopes. *Journal of Marine Science and Engineering* **2019**, *7*, 10. Number: 1 Publisher: Multidisciplinary Digital Publishing Institute, doi:10.3390/jmse7010010.
6. Tomás, R.; Romero, R.; Mulas, J.; Marturià, J.J.; Mallorquí, J.J.; Lopez-Sanchez, J.M.; Herrera, G.; Gutiérrez, F.; González, P.J.; Fernández, J.; Duque, S.; Concha-Dimas, A.; Cocksley, G.; Castañeda, C.; Carrasco, D.; Blanco, P. Radar interferometry techniques for the study of ground subsidence phenomena: a review of practical issues through cases in Spain. *Environmental Earth Sciences* **2014**, *71*, 163–181. Company: Springer Distributor: Springer Institution: Springer Label: Springer Number: 1 Publisher: Springer Berlin Heidelberg, doi:10.1007/s12665-013-2422-z.
7. Seidel, M.; Marzahn, P.; Ludwig, R. Monitoring of Sea Dike Structures by the Means of Combined StaMPS Multi-temporal InSAR Approach. *Procedia Computer Science* **2016**, *100*, 1147–1154. https://doi.org/10.1016/j.procs.2016.09.268.
8. Sub-seasonal Levee Deformation Observed Using Satellite Radar Interferometry to Enhance Flood Protection | Scientific Reports.
9. Mirzaee, S.; Amelung, F.; Fattahi, H. Non-linear phase linking using joined distributed and persistent scatterers. *Computers & Geosciences* **2023**, *171*, 105291. doi:10.1016/j.cageo.2022.105291.
10. Fattahi, H.; Agram, P.; Simons, M. A Network-Based Enhanced Spectral Diversity Approach for TOPS Time-Series Analysis. *IEEE Transactions on Geoscience and Remote Sensing* **2017**, *55*, 777–786. https://doi.org/10.1109/TGRS.2016.2614925.
11. Wu, Z.; Ellingsen, P.G.; Jia, H.; ÅDland, R.O. Tracking Volume Change of the Bulk Commodities with Interferometric SAR. IGARSS 2023 - 2023 IEEE International Geoscience and Remote Sensing Symposium; IEEE: Pasadena, CA, USA, 2023; pp. 8242–8245. doi:10.1109/IGARSS52108.2023.10281654.
12. Tirmizi, O.; Khan, S.D. Factors of Subsidence in Katy, Texas, USA. *Remote Sensing* **2023**, *15*, 4424. doi:10.3390/rs15184424.
13. Zhang, G.; Yu, Z.; Zhang, Z.; Jiang, W.; Zhang, Y. Deformation monitoring of Shuangwangcheng Reservoir based on time-series InSAR method. Fifth International Conference on Geoscience and Remote Sensing Mapping (ICGRSM 2023); Upper, M.; Alvarez, R., Eds.; SPIE: Lianyungang, China, 2024; p. 103. doi:10.1117/12.3021095.
14. Crosetto, M.; Monserrat, O.; Iglésias, R.; Crippa, B. Persistent Scatterer Interferometry: Potential, Limits and Initial C- and X-band Comparison. *Photogrammetric Engineering and Remote Sensing* **2010**.
15. Fattahi, H.; Bekaert, D.P.; Brancato, V.; Yunjun, Z.; Lu, Z.; Bato, M.G.; Kim, J.W.; Jeong, S.; Liang, K.; Sangha, S. OPERA Coregistered Single Look Complex products from Sentinel-1 data **2022**. *2022*, G45A–03. Conference Name: AGU Fall Meeting Abstracts ADS Bibcode: 2022AGUFM.G45A..03F.
16. NASA/JPL/OPERA. OPERA Coregistered Single-Look Complex from Sentinel-1 Static Layers validated product (Version 1), 2023. doi:10.5067/SNWG/OPERA_L2_CSLC-S1-STATIC_V1.
17. NASA/JPL/OPERA. OPERA Coregistered Single-Look Complex from Sentinel-1 validated product (Version 1), 2023. doi:10.5067/SNWG/OPERA_L2_CSLC-S1_V1.
18. Rosen, P.A.; Gurrola, E.M.; Agram, P.; Cohen, J.; Lavalle, M.; Riel, B.V.; Fattahi, H.; Aivazis, M.A.; Simons, M.; Buckley, S.M. The InSAR Scientific Computing Environment 3.0: A Flexible Framework for NISAR Operational and User-Led Science Processing. IGARSS 2018 - 2018 IEEE International Geoscience and Remote Sensing Symposium; IEEE: Valencia, 2018; pp. 4897–4900. doi:10.1109/IGARSS.2018.8517504.
19. Gisinger, C.; Libert, L.; Marinkovic, P.; Krieger, L.; Larsen, Y.; Valentino, A.; Breit, H.; Balss, U.; Suchandt, S.; Nagler, T.; Eineder, M.; Miranda, N. The Extended Timing Annotation Dataset for Sentinel-1—Product

Description and First Evaluation Results. *IEEE Transactions on Geoscience and Remote Sensing* **2022**, *60*, 1–22. doi:10.1109/TGRS.2022.3194216.

20. Guarnieri, A.M.; Tebaldini, S. On the Exploitation of Target Statistics for SAR Interferometry Applications. *IEEE Transactions on Geoscience and Remote Sensing* **2008**, *46*, 3436–3443. doi:10.1109/TGRS.2008.2001756.
21. Ansari, H. Synthetic Aperture Radar Interferometry.
22. Ansorena, I.L. Analysing the maritime network of the port of Algeciras Bay. *World Review of Intermodal Transportation Research* **2020**, *9*, 245–263. Publisher: Inderscience Publishers, doi:10.1504/WRITR.2020.108222.
23. Alfonso, C. "Gateway" City and Nexus Between Two Continents: The Port City of Algeciras. *Port Cities as Areas of Transition*. doi:10.14361/9783839409497-006.
24. Acosta, M.; Coronado, D.; Mar Cerban, M. Port competitiveness in container traffic from an internal point of view: the experience of the Port of Algeciras Bay. *Maritime Policy & Management* **2007**, *34*, 501–520. Publisher: Routledge _eprint: https://doi.org/10.1080/03088830701585381, doi:10.1080/03088830701585381.
25. Gil-Ropero, A.; Cerban, M.; Turias, I.J. Analysis of the Global and Technical Efficiencies of Major Spanish Container Ports. *International Journal of Transport Economics / Rivista internazionale di economia dei trasporti* **2015**, *42*, 377–407. Publisher: Accademia Editoriale.
26. Costantini, M.; Minati, F.; Trillo, F.; Ferretti, A.; Novali, F.; Passera, E.; Dehls, J.; Larsen, Y.; Marinkovic, P.; Eineder, M.; Brcic, R.; Siegmund, R.; Kotzerke, P.; Probeck, M.; Kenyeres, A.; Proietti, S.; Solari, L.; Andersen, H.S. European Ground Motion Service (EGMS). 2021 IEEE International Geoscience and Remote Sensing Symposium IGARSS; IEEE: Brussels, Belgium, 2021; pp. 3293–3296. doi:10.1109/IGARSS47720.2021.9553562.
27. European Environment Agency. European Ground Motion Service: Basic 2018-2022 (vector), Europe, yearly, Oct. 2023, 2023. doi:10.2909/1B2EB0D6-8C3A-4DE2-B99D-10A30079F3CC.
28. European Space Agency.; Airbus. Copernicus DEM, 2022. Institution: European Space Agency, doi:10.5270/ESA-c5d3d65.
29. Gisinger, C.; Schubert, A.; Breit, H.; Garthwaite, M.; Balss, U.; Willberg, M.; Small, D.; Eineder, M.; Miranda, N. In-Depth Verification of Sentinel-1 and TerraSAR-X Geolocation Accuracy Using the Australian Corner Reflector Array. *IEEE Transactions on Geoscience and Remote Sensing* **2021**, *59*, 1154–1181. doi:10.1109/TGRS.2019.2961248.
30. Maurer, J.; Bekaert, D.; Sangha, S.; Hamlington, B.; Marshak, C.; Lei, Y.; Kumar, P.; Fattahi, H. RAiDER: Raytracing Atmospheric Delay Estimation for RADAR **2021**. *2021*, G44A–07. Conference Name: AGU Fall Meeting Abstracts ADS Bibcode: 2021AGUFM.G44A..07M.
31. Hersbach, H.; Bell, B.; Berrisford, P.; Hirahara, S.; Horányi, A.; Muñoz-Sabater, J.; Nicolas, J.; Peubey, C.; Radu, R.; Schepers, D.; Simmons, A.; Soci, C.; Abdalla, S.; Abellan, X.; Balsamo, G.; Bechtold, P.; Biavati, G.; Bidlot, J.; Bonavita, M.; De Chiara, G.; Dahlgren, P.; Dee, D.; Diamantakis, M.; Dragani, R.; Flemming, J.; Forbes, R.; Fuentes, M.; Geer, A.; Haimberger, L.; Healy, S.; Hogan, R.J.; Hólm, E.; Janisková, M.; Keeley, S.; Laloyaux, P.; Lopez, P.; Lupu, C.; Radnoti, G.; De Rosnay, P.; Rozum, I.; Vamborg, F.; Villaume, S.; Thépaut, J. The ERA5 global reanalysis. *Quarterly Journal of the Royal Meteorological Society* **2020**, *146*, 1999–2049. doi:10.1002/qj.3803.
32. Noll, C.E. The crustal dynamics data information system: A resource to support scientific analysis using space geodesy. *Advances in Space Research* **2010**, *45*, 1421–1440. doi:10.1016/j.asr.2010.01.018.
33. Ferretti, A.; Fumagalli, A.; Novali, F.; Prati, C.; Rocca, F.; Rucci, A. A New Algorithm for Processing Interferometric Data-Stacks: SqueeSAR. *IEEE Transactions on Geoscience and Remote Sensing* **2011**, *49*, 3460–3470. doi:10.1109/TGRS.2011.2124465.
34. Agram, P.S.; Warren, M.S.; Calef, M.T.; Arko, S.A. An Efficient Global Scale Sentinel-1 Radar Backscatter and Interferometric Processing System. *Remote Sensing* **2022**, *14*, 3524. doi:10.3390/rs14153524.
35. Yunjun, Z.; Fattahi, H.; Pi, X.; Rosen, P.; Simons, M.; Agram, P.; Aoki, Y. Range Geolocation Accuracy of C-/L-Band SAR and its Implications for Operational Stack Coregistration. *IEEE Transactions on Geoscience and Remote Sensing* **2022**, *60*, 1–19. doi:10.1109/TGRS.2022.3168509.
36. Zebker, H.A.; Goldstein, R.M. Topographic mapping from interferometric synthetic aperture radar observations. *Journal of Geophysical Research* **1986**, *91*, 4993. doi:10.1029/JB091iB05p04993.
37. OPERA CSLC-S1 Static Layers Product Description, 2023.
38. Prats-Iraola, P.; Scheiber, R.; Marotti, L.; Wollstadt, S.; Reigber, A. TOPS Interferometry With TerraSAR-X. *IEEE Transactions on Geoscience and Remote Sensing* **2012**, *50*, 3179–3188. doi:10.1109/TGRS.2011.2178247.

39. Bara, M.; Moreira, A. Interferometric SAR Signal Analysis in the Presence of Squint. *IEEE TRANSACTIONS ON GEOSCIENCE AND REMOTE SENSING* **2000**, *38*.
40. Rodriguez-Cassola, M.; Prats-Iraola, P.; De Zan, F.; Scheiber, R.; Reigber, A.; Geudtner, D.; Moreira, A. Doppler-Related Distortions in TOPS SAR Images. *IEEE Transactions on Geoscience and Remote Sensing* **2015**, *53*, 25–35. doi:10.1109/TGRS.2014.2313068.
41. *EUSAR 2014; 10th European Conference on Synthetic Aperture Radar; Proceedings of: date 3-5 June 2014*; IEEE: Piscataway, N.J., 2014. OCLC: 893191408.
42. Milbert, D. Solid: Solid Earth Tide, 2018.
43. Ansari, H.; Adam, N.; Brcic, R. Amplitude time series analysis in detection of persistent and temporal coherent scatterers. 2014 IEEE Geoscience and Remote Sensing Symposium; IEEE: Quebec City, QC, 2014; pp. 2213–2216. doi:10.1109/IGARSS.2014.6946908.
44. De Zan, F.; Lopez-Dekker, P. SAR Image Stacking for the Exploitation of Long-Term Coherent Targets. *IEEE Geoscience and Remote Sensing Letters* **2011**, *8*, 502–506. doi:10.1109/LGRS.2010.2089494.
45. Guarnieri, A.; Tebaldini, S. Hybrid CramÉr–Rao Bounds for Crustal Displacement Field Estimators in SAR Interferometry. *IEEE Signal Processing Letters* **2007**, *14*, 1012–1015. doi:10.1109/LSP.2007.904705.
46. Lanari, R.; Mora, O.; Manunta, M.; Mallorqui, J.; Berardino, P.; Sansosti, E. A small-baseline approach for investigating deformations on full-resolution differential SAR interferograms. *IEEE Transactions on Geoscience and Remote Sensing* **2004**, *42*, 1377–1386. doi:10.1109/TGRS.2004.828196.
47. Ansari, H.; De Zan, F.; Bamler, R. Efficient Phase Estimation for Interferogram Stacks. *IEEE Transactions on Geoscience and Remote Sensing* **2018**, *56*, 4109–4125. doi:10.1109/TGRS.2018.2826045.
48. Ansari, H.; De Zan, F.; Bamler, R. Sequential Estimator: Toward Efficient InSAR Time Series Analysis. *IEEE Transactions on Geoscience and Remote Sensing* **2017**, *55*, 5637–5652. doi:10.1109/TGRS.2017.2711037.
49. Ferretti, A.; Prati, C.; Rocca, F. Permanent scatterers in SAR interferometry. *IEEE Transactions on Geoscience and Remote Sensing* **2001**, *39*, 8–20. doi:10.1109/36.898661.
50. Navneet, S.; Kim, J.W.; Lu, Z. A New InSAR Persistent Scatterer Selection Technique Using Top Eigenvalue of Coherence Matrix. *IEEE Transactions on Geoscience and Remote Sensing* **2018**, *56*, 1969–1978. doi:10.1109/TGRS.2017.2771386.
51. Chen, C.W.; Zebker, H.A. Network approaches to two-dimensional phase unwrapping: intractability and two new algorithms. *Journal of the Optical Society of America A* **2000**, *17*, 401. doi:10.1364/JOSAA.17.000401.
52. Yunjun, Z.; Fattahi, H.; Amelung, F. Small baseline InSAR time series analysis: Unwrapping error correction and noise reduction. *Computers & Geosciences* **2019**, *133*, 104331. doi:10.1016/j.cageo.2019.104331.
53. Observational Products for End-Users from Remote Sensing Analysis (OPERA) - Product Validation Plan. V1.5.
54. Bekaert, D. OPERA Analysis-Ready SAR and Optical Products for Mapping Water Extent, Disturbance, and Displacement at Continental to Near-Global Scales, 2023.
55. Dheenathayalan, P. Optimizing the exploitation of persistent scatterers in satellite radar interferometry. PhD thesis, Delft University of Technology. doi:10.4233/UUID:AA1EF96F-4DA9-41FF-BFF8-30186EF2A541.